Signal-based analysis of the dynamic behaviour of the system in inertia friction welding and its impact on part contact evolution

Luca Raimondi , Christopher J. Bennett [*], Andres Gameros , Dragos Axinte

Rolls-Royce UTC in Manufacturing and On-Wing Technology, The University of Nottingham, NG7 2RD, UK

ARTICLE INFO

ABSTRACT

Inertia friction welding (IFW) is a process used to create joints with high geometrical accuracy and near net shape form. To cope with the complex phenomena occurring during welding, the majority of available studies have analysed the interaction of the workpieces to be joined under simplified conditions, in which the influence of machine assembly tolerances, spindle dynamics and system compliance have been neglected. Among the dimensional properties, the headstock-tailstock concentricity is particularly important to assess the conformity of the weld, for this reason, a novel approach was developed to investigate the physical causes behind the evolution of the radial misalignment between the two workpieces, conventionally referred to as radial runout. First an inverse approach to evaluate the equivalent pressure distribution at the weld interface and the equivalent process loads was implemented starting from the experimental data of radial runout, headstock angular speed and strain extracted with a custom monitoring system during a set of steel welds. The results showed a large variability of the pressure distribution in circumferential direction and non-axisymmetric load components in particular during the conditioning and burnoff phases. Then, the equivalent process loads were used as an input for a Timoshenko beam dynamic representation of the spindle. A good agreement between the model and the experimental data was observed with an average relative error in the radial runout of 0.085. From these results, it was possible to conclude that the lack of axisymmetry in the load components has to be attributed mainly to the misalignment between two workpieces, while the irregular runout to compliance of the system to the non-ideal process loads.

1. Introduction

The need for high-quality joints in materials difficult to weld, such as nickel-based superalloys, has encouraged the research in solid-state friction-based processes. Among these, Inertia Friction Welding (IFW) has found several applications due to its good repeatability, ease of automation, no requirement for shielding gas, filler material or vacuum, and a lack of bulk melting [1]. IFW is conventionally divided into the three stages, shown in Fig. 1, namely: conditioning, burnoff and consolidation.

The conditioning phase extends from the moment at which the two workpieces come into contact, conventionally referred to as part contact, to the instant in which the two workpieces are in complete contact, with all the surface imperfections abraded by friction, and the bulk deformation starts to occur. The torque caused by the friction between the two workpieces first increases due to the progressive increase in the contact area and then drops due to the localised softening and consequent switch from a Coulomb friction

---

Nomenclature

δ_r	Displacement in radial direction
$\delta_{x,y}$	Displacement in the x and y directions
$\in$	Load distribution factor
$[C]$	Damping matrix
$[G]$	Gyroscopic matrix
$[M]$	Mass matrix
$\{L\}$	Loads vectors
$\{q\}$	Coordinates vector
μ	Equivalent friction coefficient
Ω	Angular rotation of the shaft
ω_0	Initial angular speed
ρ	Density
θ_i	Angular coordinate
$\theta_{x,y}$	Rotation about the x and y axis
A	Cross section
F_r	Radial load acting on the bearing
E	Young's modulus
F_{A_i}	Axial load contributions
$F_{A_{tot}}$	Overall axial load
$F_{b_{A,B}}$	Reaction force of the supports
$F_{x,y}$	Load in X and Y direction
G	Shear modulus
I	Moment of inertia
J	Polar moment of inertia
r_i	Radial coordinate
K_n	Deflection constant
k_s	Transverse shear form factor
L_1	Distance between the supports
L_g	Position of the centre of mass
$M_{x,y}$	Moment in X and Y direction
$m_{x,y}$	Distributed moments per unit length in the x and y directions
n	Bearing constant
P	Axial load
P_d	Diametral clearance
$p_{x,y}$	Distributed loads per unit length in the x and y directions
J_r	Radial load integral
T	Experimental torque
t	Time (Independent variable)
W	Weight of the spindle
$x_{A,B}$	Displacement of the supports
Z	Number of rolling elements

behaviour to one based on the shear stress of the material being welded. The burnoff phase is characterised by a full plasticisation of the welding interface and constant torque, until it increases in the consolidation phase when the junction cools down and acquires strength. The IFW process can be controlled using three control parameters: initial angular speed (ω_0), flywheel inertia (I) and axial load (P), with the initial speed and inertia determining the available energy for the weld while the axial load the rate of energy input [2]. Fig. 2 shows a popular build for inertia welders. The spindle side of the machine includes shaft and flywheels (2); two support structures (1, 3) used as housing for the axial bearing (AB), the radial bearings (RB), the hydraulic motor that accelerates the spindle; the tooling (4) used to constrain the spindle side workpiece. It is important to note that, unlike other machine configurations, this flywheel arrangement greatly reduces the compliance of the system under the weight of its elements. The fixture side of the IFW machine includes the ram (8), which exerts the axial load during the weld, and the sliding structure (5), which carries the tooling (4) that holds the second workpiece. Finally, the tie rods (6) that connect the spindle and fixture sides of the machine add rigidity to the system.

It is easy to observe how the machine spindle represents a complex rotordynamic system, in which the shaft, supported by a combination of radial and axial bearings, carries flywheels of large mass and inertia, rotates at relatively high and non-constant

angular speed and is subject to significantly high process loads. An understanding of the dynamic behaviour of the machine spindle would be greatly beneficial in assessing its response to the welding and possible effects on the process outcomes, as it already happens for other applications in which researchers have studied the complex behaviour of rotors since the late nineteenth century [3,4]. The most basic system that can be studied is a Jeffcott rotor, in which a large mass and inertia disk is mounted on a massless flexible shaft supported by rigid bearings [5]. Although the simplicity of this model makes it particularly suitable for analytical analysis [6], it also limits its practical application, for this reason, a significant effort has been made to improve the modelling of the key elements, i.e. bearings and shaft, and their coupling.

Restricting the analysis to rolling elements bearings, five approaches can be used to describe their behaviour: lumped-parameter, quasi-static, quasi-dynamic, dynamic and FE based [3]. Among these, the quasi-static approach, based on the force and moment equilibriums for the rolling elements and the bearing races, became widely adopted due to its relative simplicity and capability to obtain an explicit formulation of the bearing stiffness [3]. An example of a popular quasi-static model is the one proposed by Harris, which allows to include different types of load conditions [7].

When the rotor is considered in its entirety, i.e. combination of bearings and shaft, approaches based on the Jeffcott rotor, rigid shaft, transfer matrix method and FE method have been employed [3]. In recent years, with high performance computing systems more broadly available, FE models have become more attractive to obtain accurate solutions for complex systems. Among these, beam element approaches have been widely used due to an excellent trade-off between accuracy and calculation time, while 3D solid element models have been reserved for particularly complex systems or when dealing with asymmetric and anisotropic cases [5]. Machine tools represent an important category of rotordynamic systems with a deep industrial impact, for which it has been long recognised how the quality measures, e.g. dimensional accuracy and surface finish, are closely related to the dynamic characteristic of the associated spindle-bearing system [8].

One of the first machining processes studied in terms of dynamic behaviour was turning, with Chen et al. [9] that, understanding the importance of the setup on the accuracy of the machining outcomes, proposed a coupled thermo-mechanical FE model to optimise the design of the spindle, bearings and casing of a lathe. Altintas and Cao [10,11] analysed the natural frequencies, mode shapes and frequency response function of a machine tool under simulated cutting conditions (virtual cutting). The model used Timoshenko beams for the spindle, including both centrifugal force and gyroscopic effects, while Jones' model was used for the bearings. Following studies extended the analysis to consider the effect of different preloads on the bearings [12,13] and the damping and stiffness of the tool holder-spindle/tool-tool holder interfaces [14]. The dynamic study of spindle-tool systems has proven particularly important for high-speed milling, for which several numerical models based on Timoshenko beams FE models and bearings with non-linear stiffness have been implemented to analyse the chatter stability of the system. These studies showed that while negligible at relatively low speed, gyroscopic effects and dynamic stiffness drop, due to centrifugal force, become predominant at high speeds [15–17]. Finally, additional studies have indicated how the stability of rotor-bearing systems can be affected by the external loads applied to the spindle [18] and bearing related parameters, such as race waviness, elastohydrodynamic lubrication and clearance [19,20].

From this analysis it appears how the dynamic behaviour of the manufacturing set-up plays a fundamental role on the system response to the process conditions and, consequently, on the quality of the outcomes [21]. However, even if an inertia welder presents the dynamic challenges previously highlighted, no study in public literature has been presented to understand the actual transient loading conditions of the machine spindle and how the system reacts to them. This research gap is particularly problematic having observed a non-negligible runout during welding trials. In fact, IFW is a near net shape process for which the geometrical accuracy of the weld is of primary importance and the runout plays an important role among the geometrical parameters measured at the end of the process to determine the conformance of the weld. In addition, issues of runout and imperfect alignment between the two workpieces could induce a non-constant pressure and, consequently, temperature at the weld interface that can result in hot spots, non-homogenous microstructure and, ultimately, process variability. Therefore, starting from the experimental data of headstock-tailstock concentricity, headstock angular speed and strain extracted with a custom monitoring system during a set of steel welds, a novel
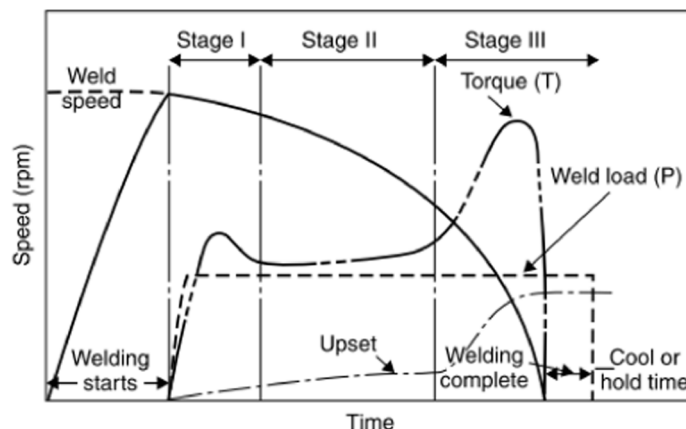
Fig. 1. Welding stages of IFW and corresponding process variables (Adapted from [1]).
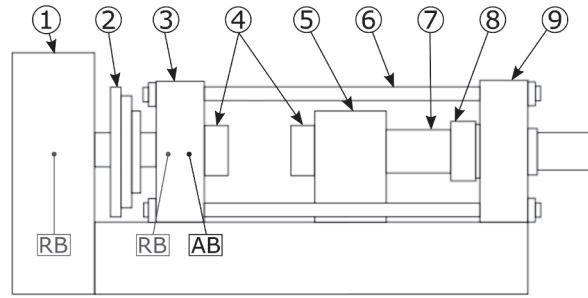
1: Motor and bearing housing; 2: Flywheels; 3: Spindle support structure; 4: Tooling; 5: Fixture slide structure;
6: Tie rod; 7: Shaft; 8: Ram; 9: Fixture support structure; RB: Radial bearing; AB: Axial bearing

Fig. 2. Schematic of an inertia welder (Based on an MTI's proprietary design).

approach to determine the equivalent process loads which occur during a weld is proposed. Then, the loads are applied to a 3D beam dynamic representation of the machine spindle with the radial supports modelled according to Harris theory. The main contributions of the article can be summarised as follows:

1. Develop an approach to evaluate the equivalent pressure distribution at the weld interface and study its evolution throughout the process;
2. Convert the pressure distribution into equivalent process loads and assess the validity of the axisymmetric assumption conventionally adopted to study IFW;
3. Study the evolution of the headstock-tailstock concentricity during welding and understand the physical causes behind its behaviour, a necessary step in improving weld quality an repeatability.

2. Methodology

To obtain an understanding of the physical causes for the runout during the process, a novel methodology to compute the non-axisymmetric loads that originate when the two workpieces interact in non-ideal conditions was developed. The loads were used as input for a 3D dynamic beam representation of the machine spindle, the outcomes of which were validated against the experimental data of strain and radial runout extracted with a custom monitoring system [22]. Fig. 3 provides an overview of the algorithm developed and outlines the two main steps of the approach:

Step 1 – Calculation of the equivalent loads originated by the interaction of the workpieces during the welding. Values of pressure distribution at the weld interface (1.2) were first obtained from the experimental data measured with a monitoring system (1.1). These were converted into equivalent process loads and used as input for an optimisation which adjusted the values of pressure to minimise the error in two objective functions: an FE model of the monitoring system (1.3), in which the strain induced by the equivalent loads were compared to the experimental strain and an analytical static representation of the spindle (1.4), in which the deflection induced by the equivalent loads were compared to the experimental data of runout.

Step 2 – Dynamic evolution of the runout during the process. Firstly, a 3D dynamic representation of the machine spindle was developed using Timoshenko beam elements and Harris' theory to model the radial supports, then the equivalent loads computed in step 1 (I.1) and the experimental angular speed were applied to the model. Finally, the model's outcomes were compared against the experimental data of runout and the static representation developed in step 1 (1.4).

2.1. Loads induced by non-axisymmetric conditions

The process loads, in terms of torque and axial load, conventionally obtained with the sensors embedded in the inertia welder, are presented in Fig. 1. These values, however, are intrinsically smoothed by the remote location of the sensors relative to the weld zone, which induces a sensitivity loss to the local phenomena induced by the interaction of the workpieces. To address this limitation, a novel approach to compute equivalent process loads, starting from the experimental strain conditions near the weld zone, was developed. Ultimately, the approach aims to provide a more accurate representation of the loads generated during a weld when the two workpieces interact under non-idealised conditions.

The approach is based on the observation that the process loads, along with the weld evolution, are guided by the conditions at the interface of the two workpieces. For this reason, the values of axial load at specific circumferential positions (F_{A_i}) were interpolated over the welding surface, discretised with a structured mesh and finally used to compute the equivalent loads ($F_{A_{tot}}, F_x$ and F_y) and moments (M_x, M_y), as shown in Fig. 4 and detailed in Eq. (1)–(5).

$$F_{A_{tot}}(t) = \sum F_{A_i}(t) \tag{1}$$
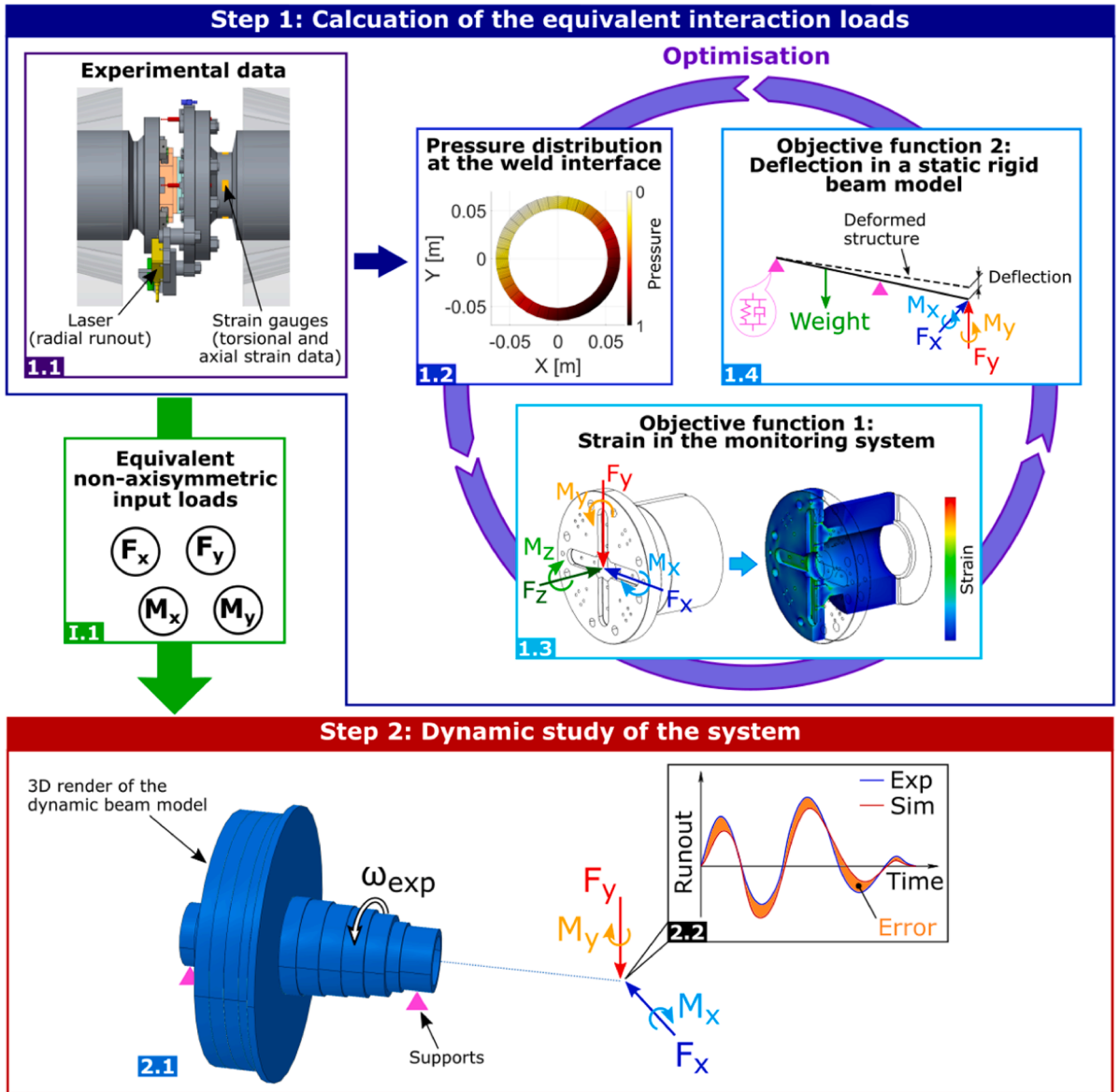
Fig. 3. Schematic representation of the approach used for the analysis of the runout evolution during the welding.

$$M_x(t) = \sum F_{A_i}(t) \cdot r_i \cdot \sin\theta_i \tag{2}$$

$$M_y(t) = \sum F_{A_i}(t) \cdot r_i \cdot \cos\theta_i \tag{3}$$

Tangential direction

$$F_x = \sum \mu(t) F_{A_i} \cos\left(\theta_i + \frac{\pi}{2}\right) \tag{4}$$

$$F_y = \sum \mu(t) F_{A_i} \sin\left(\theta_i + \frac{\pi}{2}\right) \tag{5}$$

The tangential loads expressed by Eq. (5) make use of the concept of an equivalent friction coefficient [23] and were calculated from the axial loads contributes and the experimental torque (*T*) as:

$$\mu(t) = \frac{\sum F_{A_i}(t) \cdot r_i}{T(t)} \tag{6}$$
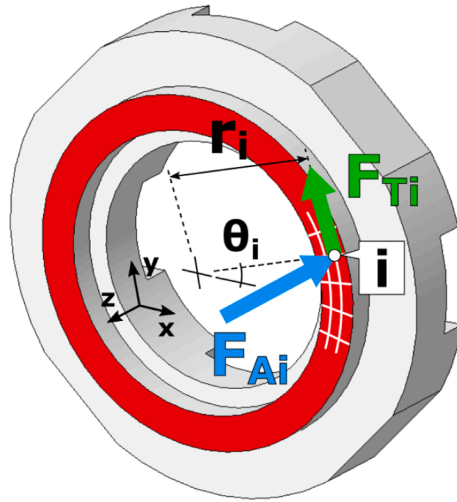
Fig. 4. Graphic representation of the axial and tangential load contributes on the welding surface of the workpiece.

It is important to note two aspects, firstly the experimental measurements used as the input to compute the axial contribution over the welding interface provide just a coarse approximation of the actual pressure field due to the limited number of sensors which can be installed in the monitoring system. Secondly, the measurements of axial load with strain gauges aligned with the axis of the spindle are not sufficient to fully decouple the contribution of radial loads and moments, therefore multiple combinations of loads can bring to the same value of strain experimentally monitored. For this reason, the load components cannot be obtained directly from the experimental measurements but rather the equivalence between the model and the actual system is ensured with an optimisation algorithm that iteratively updates the load components to minimise the difference in strain and radial runout.

To reduce the computational cost of the optimisation, rather than optimise the value of each axial contribution, a third order Fourier series was used to describe the axial load variation around the weld interface. The choice of a Fourier series over other fit functions is justified by the expected fixture/spindle misalignment to be in phase with the angular rotation of the spindle and, consequently, the pressure over the weld surface to vary periodically. The parameters of the Fourier series were updated by the optimisation algorithm so that the value of the two objective functions were minimised. The first objective function compares the experimental strain at different points in the monitoring system with the solution from a 3D FE model of the backup when the equivalent loads are applied (1.4 in Fig. 3) while the second compares the experimental runout of the spindle with the displacement induced in a static beam that represents the spindle (1.3 in Fig. 3). Neglecting the axial contribution and analysing separately the two orthogonal directions X and Y, the problem becomes planar and can be studied with the model in Fig. 5 for which the load and moment equilibrium equations can be respectively written as:

$$F_{b_A}(x_A) - W + F_{b_B}(x_B) = F \tag{7}$$

$$-W \cdot L_g + F_{b_B}(x_B) \cdot L_1 = F \cdot L + M \tag{8}$$

where F_{b_A} and F_{b_B} are the reaction forces of the rear and front supports respectively, x_A and x_B the displacements of the shaft at the support locations, W the weight of the spindle, F the equivalent radial process load, L_g the position of the centre of mass of the spindle shaft, L_1 the distance between the supports and L the overall length of the spindle shaft, including the tooling and workpiece. All the dynamic effects, such as spindle rotation and the damping of the supports, were neglected in this model, however, their quantitative influence on the system response was investigated analysing the rotordynamics of the spindle, as it will be shown in Section 2.2. IFW machines conventionally have a combination of bearings to support the spindle [2] and for this study a single cylindrical roller bearing was assumed for the rear support and a combination of a deep groove ball bearing and a cylindrical roller bearing for the front support.
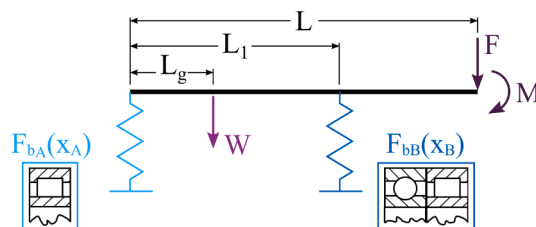
Fig. 5. Static analytical model for the study of the spindle deflection with details of the bearings adopted for the rear and front supports.

Using the approach presented in Harris and Kotzalas [7], the relationship between the radial load acting on the bearing (F_r) and the radial displacement of the bearing (δ_r) can be obtained summing the components acting on each rotating element as:

$$F_r = ZK_n \left(\delta_r - \frac{1}{2}P_d \right)^n J_r(\epsilon) \qquad (9)$$

where Z is the number of rolling elements, K_n the deflection constant that takes into account the deformation of a rolling element assuming Hertzian contact with the bearing races, P_d the diametral clearance, n a constant that depends from the type of rolling element (3/2 for ball bearings and 10/9 for roller bearings), J_r the radial load integral and ϵ the load distribution factor, which can be expressed as:

$$\epsilon = \frac{1}{2} \left(1 - \frac{P_d}{2\delta_r} \right) \qquad (10)$$

Since the radial integral is a function of ϵ, which includes δ_r, a direct solution of Eq. (9) is not possible. Therefore, when the value of external load F_r is known, the deformation of the bearing, δ_r, can be obtained by iteratively solving the equation; first a guess value of δ_r is assumed and used to compute the radial load integral, following this the value of δ_r was updated until the two sides of Eq. (9) were equal. Using the representative dimensions reported in Table 1, the radial load–displacement characteristic for the two types of bearings were computed. From these, the load–displacement characteristics for the rear and front supports were determined as shown in Fig. 6, where the front support was obtained considering a single roller bearing while the rear a combination of ball and roller bearings.

2.2. Dynamic representation of the machine spindle

To assess the influence of dynamic phenomena on the runout of the spindle, a study using the beam model presented in Fig. 7 was carried out. The system comprises: a variable section Timoshenko beam partitioned into 14 segments; the radial supports, using the same bearing configuration considered for the static model in Section 2.1; and a rigid connection beam which represents the elements between the front radial support and the workpiece (thrust bearing, tooling and the flywheels). The choice for a rigid connector rather than a flexible beam is motivated by the significantly larger stiffness of the thrust bearing and tooling compared to the shaft that supports the flywheels, which makes the deflection of these elements negligible. Table 2 summarises the geometrical details of the beam model.

The equations of motion for a rotating Timoshenko beam obtained with the Hamilton's principle when the axial and torsional contributions are neglected and the cross section, moments of inertia and length of the beam remain constant can be expressed as [24]:

$$\rho A \frac{d^2\delta_y}{dt^2} - \frac{\partial}{\partial z}\left[k_s AG \left(\frac{\partial\delta_y}{\partial z} - \theta_x \right) \right] - p_y - \Omega^2 \rho A \delta_y = 0$$

$$\rho A \frac{d^2\delta_x}{dt^2} - \frac{\partial}{\partial z}\left[k_s AG \left(\frac{\partial\delta_x}{\partial z} - \theta_y \right) \right] - p_x - \Omega^2 \rho A \delta_x = 0$$

$$\rho I \frac{d^2\theta_y}{dt^2} + \Omega\rho J \frac{d\theta_x}{dt} - EI \frac{\partial^2\theta_y}{\partial z^2} + k_s AG \left(\frac{\partial\delta_x}{\partial z} + \theta_y \right) - m_y = 0 \qquad (11)$$

$$\rho I \frac{d^2\theta_x}{dt^2} - \Omega\rho J \frac{d\theta_y}{dt} - EI \frac{\partial^2\theta_x}{\partial z^2} - k_s AG \left(\frac{\partial\delta_y}{\partial z} - \theta_x \right) - m_x = 0$$

where ρ is the density of the material, A the cross section, E the Young's modulus, G the shear modulus, J the polar momens of inertia, k_s the transverse shear form factor, $\delta_{x,y}$ the displacement in the x and y directions, $\theta_{x,y}$ the rotation about the x and y axis, and $p_{x,y}$ and $m_{x,y}$ the distributed loads and moments respectively. Using the superscript b for identifying the beam, the matrix form of Eq. (11) is:

$$[M^b]\{\ddot{q}\} - \Omega[G^b]\{\dot{q}\} + \left([K^b] - \Omega^2[M^b]_C\right)\{q\} = \{L^b\} \qquad (12)$$

Table 1
Bearing specifications

		Ball bearing	Roller bearing
Bore diameter	d	400 mm	400 mm
Outer diameter	D	600 mm	600 mm
Bearing width	w	90 mm	90 mm
Diametral clearance	P_d	100 μm	100 μm
Number of rolling elements	z	15	26
Width roller	w_r	–	50 mm
Ball diameter	d_b	60 mm	–
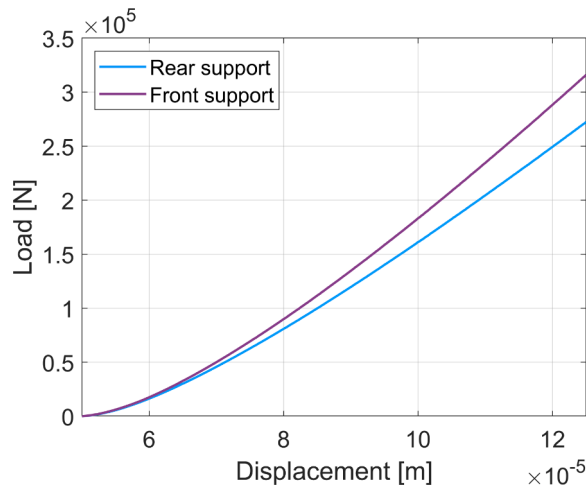
Fig. 6. Reaction load-deformation curves for the front and rear supports of the spindle shaft.
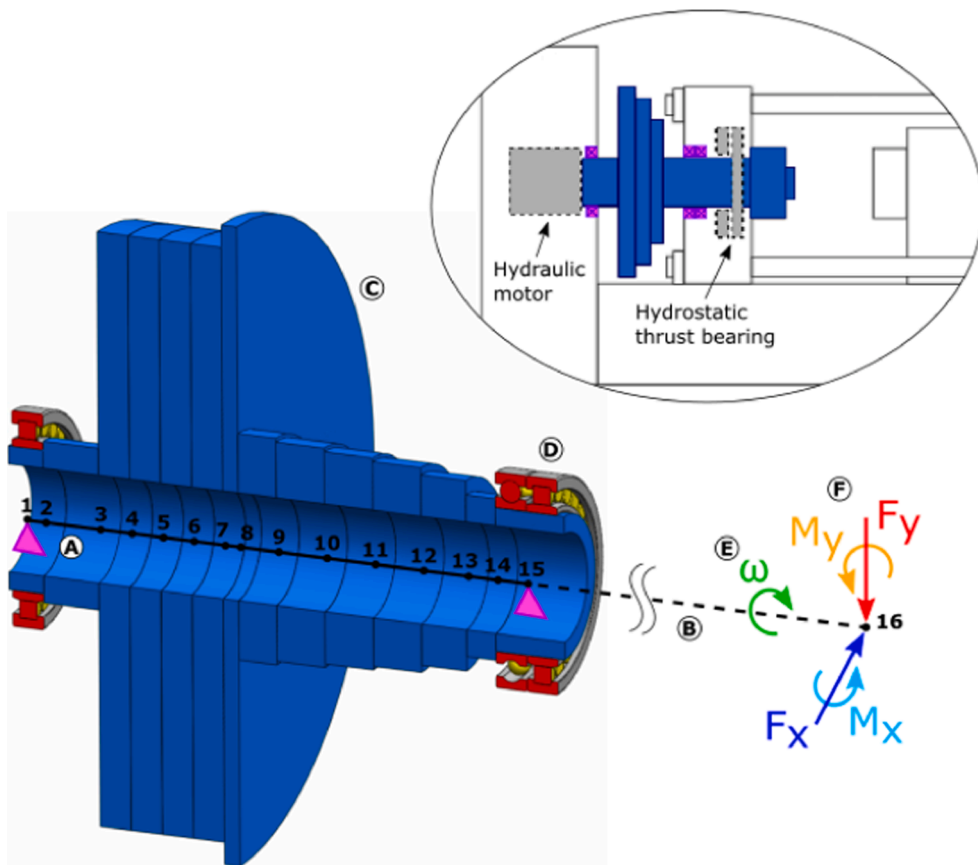
Fig. 7. Schematic of the beam model analysed for the dynamic study (A: Beam model with details of the supports and nodes; B: Rigid connector beam; C: Beam profile render; D: CAD representation of the radial supports; E: Experimental angular speed; F: Equivalent process loads computed with the procedure in Section 2.1) (Based on an MTI's proprietary design).

where $[M^b]$ is the mass matrix obtained summing the translational and rotational contributions, $[M^b]_C$ is the mass matrix used to compute the centrifugal forces, $[G^b]$ is the skew-symmetric gyroscopic matrix, $[K^b]$ is the stiffness matrix, and $\{q\}$ is the coordinate vector. The experimental angular speed of the spindle was used to define Ω, while the equivalent process loads computed in Section 2.1 were used to populate the load vector $\{L^b\}$. The matrices details can be found in previous works [24,5].

Table 2
Geometrical specifications for the beam model studied in the dynamic characterisation of the system

Segment	Nodes ID	Inner diameter	Outer diameter	Length
1	1–2	300 mm	400 mm	100 mm
2	2–3	300 mm	450 mm	160 mm
3	3–4	300 mm	1660 mm	90 mm
4	4–5	300 mm	1660 mm	90 mm
5	5–6	300 mm	1660 mm	90 mm
6	6–7	300 mm	1660 mm	90 mm
7	7–8	300 mm	1780 mm	45 mm
8	8–9	300 mm	630 mm	110 mm
9	9–10	300 mm	610 mm	140 mm
10	10–11	300 mm	590 mm	140 mm
11	11–12	300 mm	570 mm	140 mm
12	12–13	300 mm	530 mm	130 mm
13	13–14	300 mm	450 mm	90 mm
14	14–15	300 mm	400 mm	200 mm
15	15–16	– (Rigid connector)	– (Rigid connector)	2000 mm

To obtain the global equations of motion for the spindle-bearing system, it is necessary to consider also the contribution of the flywheel (superscript d) and bearings (superscript c). Modelling the flywheel as a rigid cylindrical disk with an equivalent mass and inertia, the equation of motion can be expressed as:

$$[M^d]\{\ddot{q}\} - \Omega[G^d]\{\dot{q}\} = \{L^d\} \qquad (13)$$

where $[M^d]$ is the mass matrix, $[G^d]$ the gyroscopic matrix and $\{L^d\}$ the load vector. Also in this case, the details of the matrices can be found in previous works [24,5]. The contribution of the bearings is accounted for considering the associated stiffness ($[K^c]$) and

1: Workpieces; 2: Backups; 3: Encoder; 4: Lasers; 5: Strain gauges
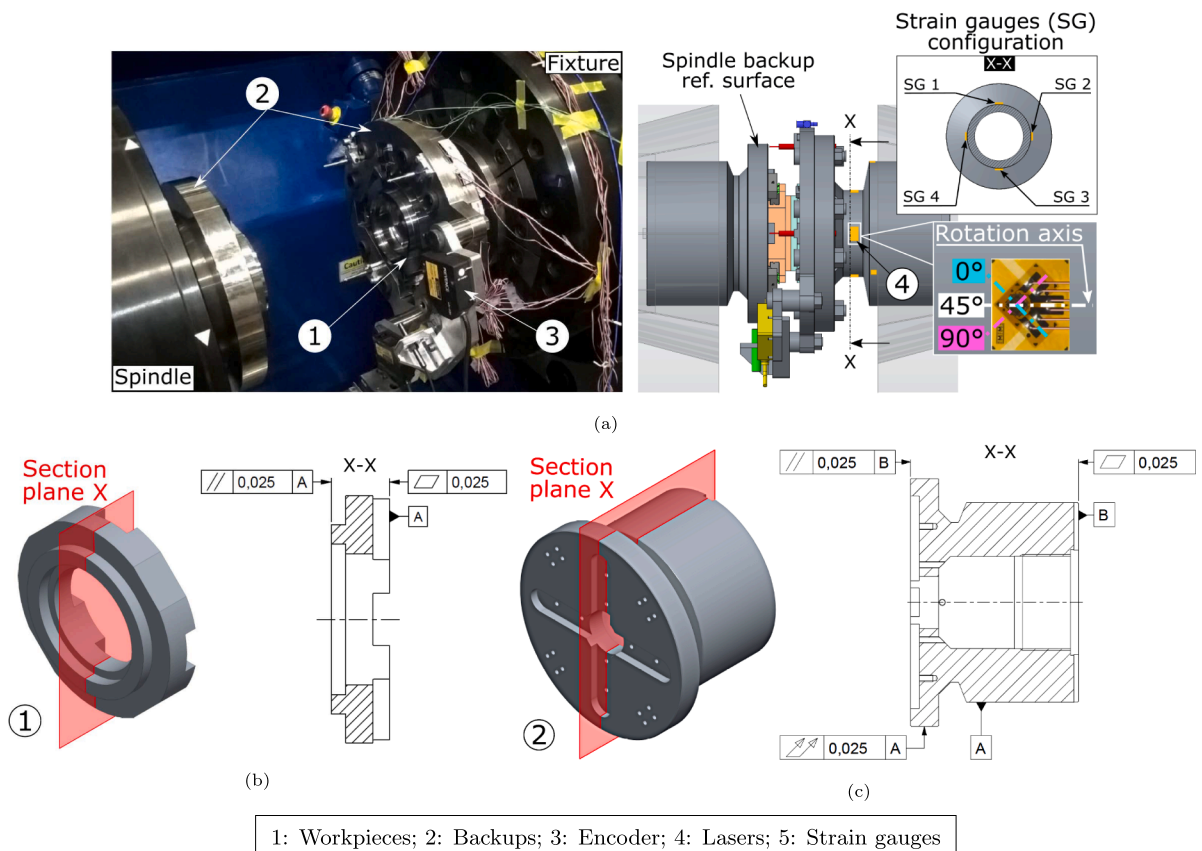
Fig. 8. Experimental set-up with details of the key elements: (a) Monitoring system and CAD representation inserted in the machine tooling with sensors and workpieces installed; (b) Detail of the key geometrical design tolerances for the workpieces; (c) Detail of the key geometrical design tolerances for the backups (spindle side backup shown).

damping ($[C^c]$) matrices. Modelling the bearings as a spring-damper system and considering only the terms along the main diagonal, the stiffness matrix was populated from the load/displacement characteristic curves presented in Section 2.1 ($k_{ii} = \partial F_{r_i}/\partial \delta_{r_i}$) while a constant value of 1000 Ns/m was considered for damping coefficients [25].

Finally, the global equations of motion in matrix form can be written as [5]:

$$[M]\{\ddot{q}\} + ([C] - \Omega[G])\{\dot{q}\} + [K]\{q\} = \{L\} \tag{14}$$

where $[M] = [M^b] + [M^d]$ is the global mass matrix, $[C] = [C^b] + [C^c]$ the global damping matrix, $[G] = [G^b] + [G^d]$ the global gyroscopic matrix, $[K] = [K^b] + [K^c] - \Omega^2 [M^b]_C$ the global stiffness matrix, and $\{L\} = \{L^b\} + \{L^d\}$ the global load vector. The resulting system of equations was solved using the finite element software Abaqus.

2.3. Experimental set-up

A set of steel welds (EN19) carried out using the same values of initial speed (ω_0), ram axial load (P) and flywheel inertia (I) was used to validate the proposed modelling approach. These were performed using a MTI-300T hybrid welder equipped with the custom monitoring system shown in Fig. 8a [22]. The monitoring system works as an interface between the machine tooling and the work-piece, serving both the purpose of fixturing for the workpiece (1) and support for the instrumentation. For this study, the output of three sensors was extracted: angular speed from the encoder (3), spindle-fixture alignment from the lasers (4) and axial and tangential strain from the strain gauges (5). The two lasers shown in Fig. 8a were precisely positioned 90° apart to define the position of two points on the spindle backup reference surface. Approximating this reference surface with a circumference, acceptable assumption considering the small circularity error of the surface (2 μm), it was possible to compute the position of the spindle backup centre with respect to the fixture side using the equations for the centre of a circumference knowing two points (P_1 and P_2) and the radius:

$$x_m = \frac{x_1 + x_2}{2}, \quad y_m = \frac{y_1 + y_2}{2} \tag{15}$$

$$q = \sqrt{(x_2 - x_1)^2 + (y_2 - y_1)^2} \tag{16}$$

$$x_c = x_m \pm \sqrt{r^2 - \left(\frac{q}{2}\right)^2} \cdot \frac{y_1 - y_2}{q}, \quad y_c = y_m \pm \sqrt{r^2 - \left(\frac{q}{2}\right)^2} \cdot \frac{x_1 - x_2}{q} \tag{17}$$

with $P_1(x_1, y_1), P_2(x_2, y_2)$ the coordinates of the two points on the circumference, $P_m(x_m, y_m)$ the middle point between P_1 and P_2, q the distance between P_1 and P_2, and $P_C(x_c, y_c)$ the coordinate of the centre of the circumference. The $\pm$ sign in Eq. (17) accounts for the existence of two circles of radius r mirrored about the line $P_1 - P_2$.

Four 0°/45°/90° 3-element stacked rectangular rosettes were installed equally spaced around the circumference, the 0° and 90° gauges for each pair of opposing rosettes (SG 1-SG 3 and SG 2-SG 4) were connected in full bridge configuration to capture the torque, while the 45° (axial) gauge from each rosette in quarter bridge configuration to measure the axial load. Ideally, one single axial gauge would be sufficient to capture the axial load, however, if the strain where the strain gauges are installed is not constant around the circumference of the backup, which is likely to happen for non-axisymmetric axial loading, a pattern of strain gauges can help in understanding the actual distribution of load. More specifically, the comparison of the reading of the four axial gauges provides in-formation about the axisymmetry of the loads while the average of their reading the mean axial load, which can be compared with the value applied by the ram.

During the design and manufacturing of the monitoring system backups and workpieces, particular attention was paid on the accuracy of the geometrical features that could affect the spindle-fixture side interaction and introduce an experimental error. As shown in Fig. 8b and c, these are flatness and parallelism between the front and rear surfaces since they have a direct effect on the desired flat-to-flat contact of the workpieces that is fundamental to avoid pressure gradients at the interface and, ultimately, hot spots. The variation from the nominal dimensions after the manufacturing was characterised using a Mitutoyo Euro-C-A121210 CMM and the results summarised in Table 3. Finally, the total runout of the spindle side backup was subtracted from the data measured with the lasers to obtain the actual orbiting of the spindle.

Table 3
Geometrical errors in the workpieces and backup measured with a Mitutoyo Euro-C-A121210 CMM, the measurements for the workpieces summarised in term of mean and standard deviation (SD)

	Workpieces	Backup spindle	Backup fixture
Flatness [μm]	5 (SD: 2)	4	4
Parallelism [μm]	5 (SD: 1)	16	18
Total runout [μm]	–	24	–

3. Results and discussion

The results obtained by applying the methodology developed to a set of steel welds will be presented in this section. First the outputs of the algorithm to compute the equivalent process loads are presented, then the process loads are applied to the dynamic representation of the machine, finally the comparison of the machine behaviour in static and dynamic conditions will allow conclusions to be drawn on the main causes behind the runout evolution during welding. While reading through the results, it is important to remember that the proposed approach aims to gain an insight into the physical phenomena connected to the runout evolution in IFW and that it should not be interpreted as a predictive model. For this reason, the results of only a few of the welds carried out will be presented as a representative case study, with the conclusions maintaining a general perspective rather than being specific to the machine setup or welding parameters.

3.1. Pressure distribution on the weld interface

Using the approach described in Section 2.1 the pressure distribution over the weld interface was computed. Fig. 9 shows the interpolated pressure fields for one of the welds at five different time instances: initial contact between the workpieces (P1), halfway through conditioning (P2), end of conditioning (P3), end of burnoff (P4), and flywheel stoppage (P5), normalised against the nominal interface pressure caused by the axial load exerted by the ram. The results show that the pressure distribution around the weld surface is not axisymmetric, with a larger variability in the initial phases compared to the end of burnoff and consolidation. This result can be explained considering how the inevitable geometrical imperfections and misalignments in the workpieces, which cause an uneven pressure distribution, get smoothed out during the conditioning and the beginning of burnoff due to the abrasion of the asperities at the weld interface. This aspect becomes clear when calculating the standard deviation of the normalised pressure around the circumference, as shown in Fig. 10. In fact, the standard variation is much larger during conditioning and burnoff, while it drops in the consolidation phase, confirming a larger dispersion from the average pressure values.

A final aspect of interest in the analysis of the pressure distribution is the position over time of the peak pressure around the
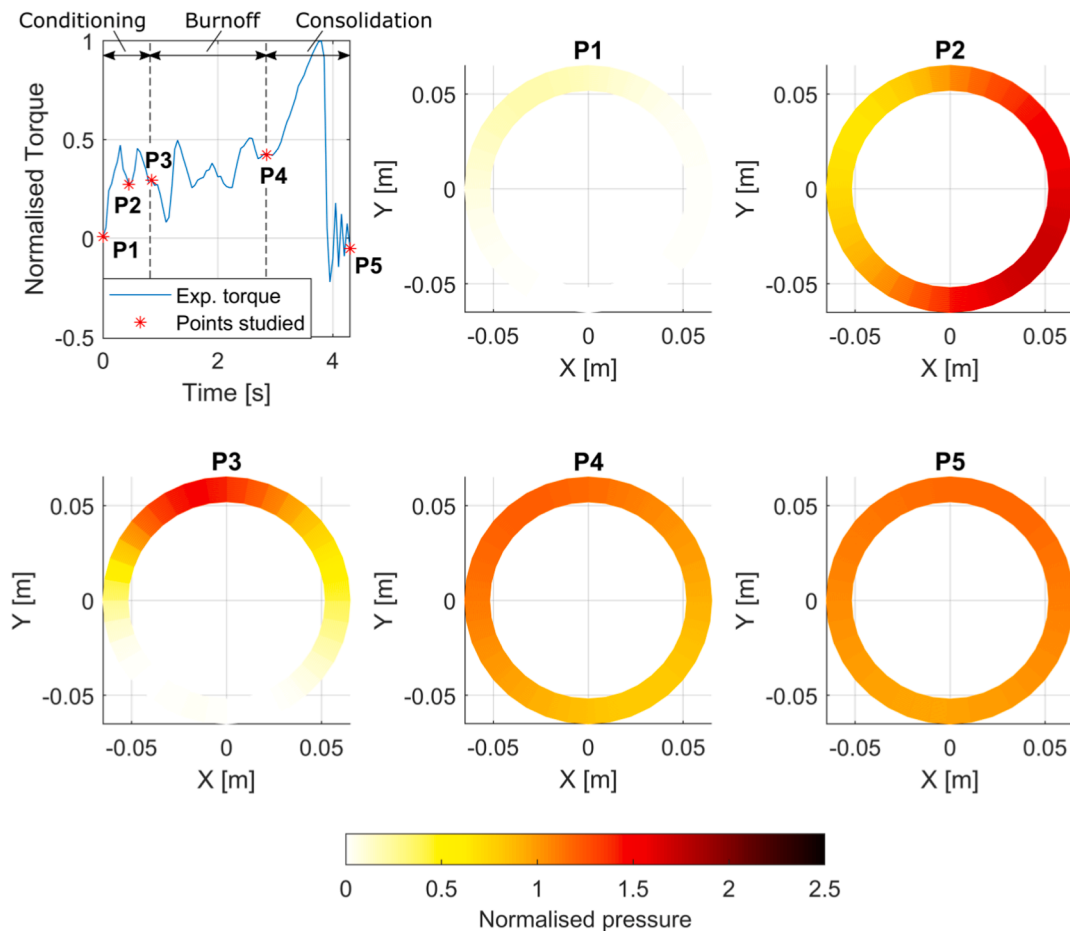
Fig. 9. Normalised pressure distribution at the weld interface at five time instances (P1, P2, P3, P4 and P5) during welding.
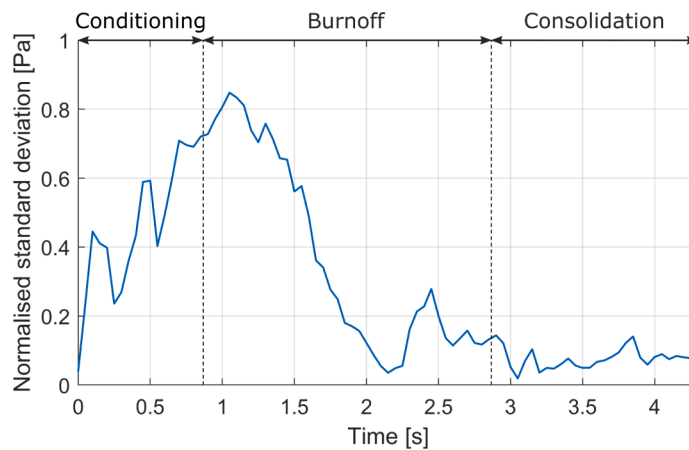
Fig. 10. Standard deviation of the pressure at the weld interface showing larger variability in the first stages of welding.

circumference, shown in Fig. 11 for three different welds completed under the same process parameters. Comparing the position of the peaks against the spindle rotations, the peak pressure location appears to be out of phase with the angular rotation of the spindle, even if a periodic behaviour is present. Combining this with the different location of the pressure peaks over time for the three cases, it is possible to conclude how this behaviour must be affected mainly by the variable conditions at the interface of the workpieces rather than the system or its set-up.

3.2. Equivalent loads and optimisation error analysis

Starting from the values of pressure distribution at the workpiece interface, the equivalent process loads were determined. Fig. 12 shows the values of force, normalised to the peak load in the axial direction (F_z), and the moments, normalised to the peak torque (M_z), for one of the welds. Large non-axisymmetric loads can be observed, with the radial forces (F_x and F_y) and moments (M_x and M_y) that show peak values 40% larger than the peak axial force (F_z) and torque (M_z) respectively. In addition, these loads follow a trend similar
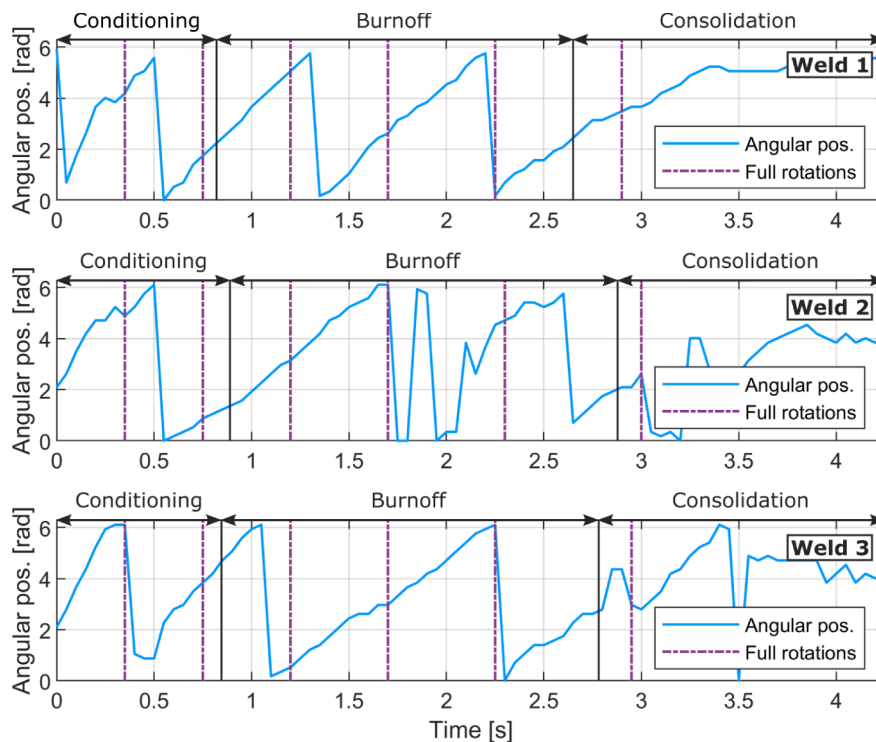
Fig. 11. Angular position of the pressure peak location around the weld interface during the welding for three welds carried out using the same process parameters, from which it is possible to observe a periodicity in the peak location but a different behaviour among the three welds.
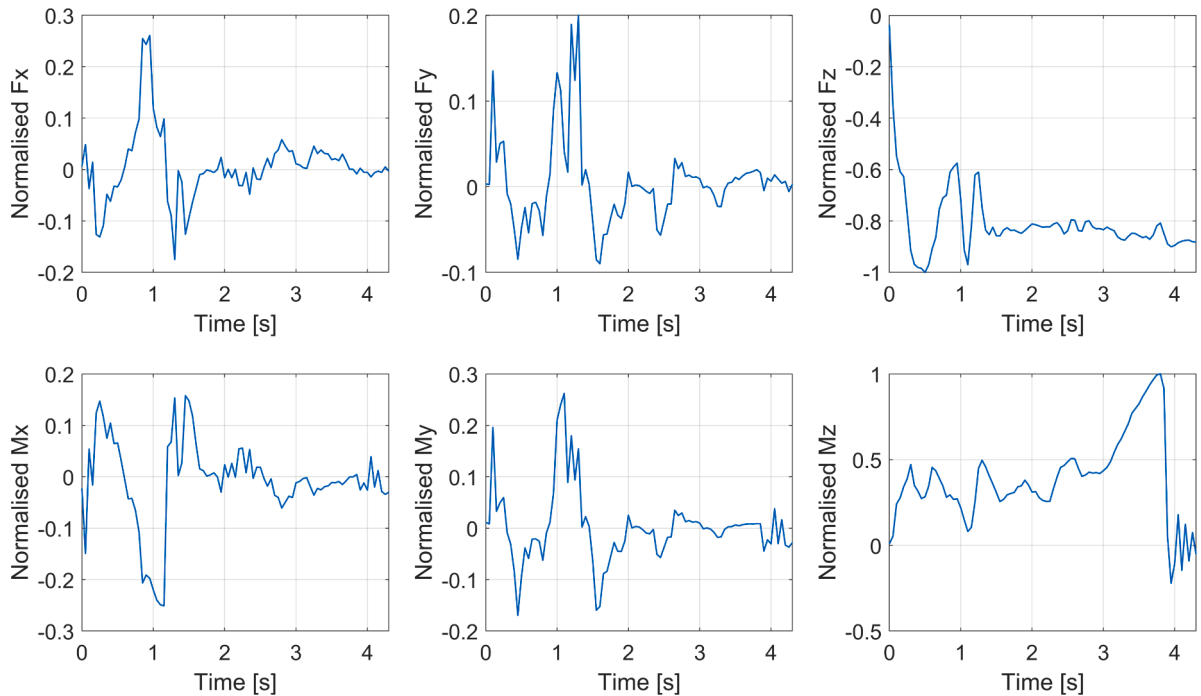
Fig. 12. Normalised equivalent loads and moments in three orthogonal directions obtained from the optimisation algorithm, from which it is possible to observe large non-axisymmetric loads (F_x, F_y, M_x and M_y).

to that of the spindle runout (Fig. 13b), with larger oscillations during the conditioning and burnoff phases rather than in the consolidation. This phenomenon can be explained by a combination of the perfect contact between the two workpieces at the end of the process and the constraining action of the weld that opposes the motion of the spindle when it acquires strength at the end of the process. Analysing the force and moment in the axial direction of the spindle, F_z and M_z, it is possible to see the characteristic behaviour typical of IFW (Fig. 1). F_z presents first a steep increase at the beginning of the process from zero to the peak load when the ram is activated and the two workpieces are brought into contact. Then, after a transitory period characterised by load fluctuations at the beginning of the burnoff phase, the load tends to stabilize. M_z shows a steep raise at the beginning of the conditioning phase, followed by a semi-stable value during the burnoff phase and a final peak when the joint starts to cool down in the consolidation phase. The oscillations observed during the burnoff phase can be connected once again to the intrinsically unstable nature of the interface conditions.

The output of the two objective functions is shown against the experimental data in Fig. 13. The first objective function shows a good agreement in term of strain for the four axial gauges, with a similar mean absolute error of 0.17 (normalised strain) for the four strain gauges, while the comparison for the torsional strain is not included because the error is two orders of magnitude smaller than the one in the axial direction and therefore negligible. This is a consequence of the approach for calculating the friction coefficient, in which the experimental torque is used to obtain an equivalent friction coefficient (Eq. (6)). Fig. 13b compares the displacement obtained from the second objective function with the experimental radial runout, in which it is possible to observe again a good match between numerical and experimental data with a mean absolute error of 0.09 (normalised runout) for both X and Y directions.

These results show that the proposed technique is capable to calculate equivalent process loads able to verify with a good approximation the equivalence in strain and displacement conditions between the numerical and the experimental data, using an inverse approach that makes use of experimental parameters easier to measure. In addition, the good match in displacement shown in Fig. 13b is of primary importance for the current investigation because the static analytical model used in the optimisation algorithm disregards the rotation of the spindle along with all possible rotordynamic phenomena. This result gives a first hint that the root cause in the runout behaviour during the welding could be related to the reaction loads caused by the interaction of the two workpieces rather than connected to the dynamics of the spindle.

3.3. Dynamic response of the system to the equivalent loads

To further investigate the influence of the loads generated by the interactions of the workpieces on the runout, the dynamic representation of the machine spindle presented in Section 2.2 was used. Fig. 14 shows the response of the dynamic model in terms of radial displacement when the experimental angular speed and the equivalent loads calculated in the previous section are taken into account and compares it with both the static solution (the second objective function of the optimisation) and the experimental radial runout. Comparing the results for three different welds completed with the same process parameters, it is possible to observe a similar

behaviour and, consequently, a good repeatability of the approach.

A very good agreement between the static and dynamic solutions can be observed, with small differences ascribable to the flexibility accounted in the Timoshenko beam elements used for the dynamic model but neglected in the rigid beam of the static one. The good agreement between the experimental data and numerical solutions supports the hypothesis presented in the previous section that the loads generated by the non-ideal interaction of the two workpieces represents the major influence on the runout evolution. This imperfect contact can be attributed to misalignment between the fixture and spindle sides as well as geometrical imperfections in the workpieces.

Fig. 15 shows the mean relative error, calculated as mean of the absolute error divided by the peak amplitude of oscillation, between static and dynamic model (E1) and between dynamic model and experimental data (E2). It is possible to observe that the error in X and Y direction is similar for each weld and the ratio between the two types of comparisons (E1 and E2) keeps a similar proportionality, suggesting once more the good repeatability of the approach. E2 can be explained with the approximations for the geometry and technical details of some element of the models (e.g. spindle shaft and bearings). However, considering the approach developed aimed to gain an insight on the physics of the process rather than be used as a predictive tool, the match with the experimental data seems appropriate.

4. Conclusions

This research challenged the popular assumption of treating IFW as a perfectly axisymmetric process, showing instead how the two workpieces tend to interact during the welding in non-ideal conditions due to the presence of small misalignments, which induce considerable non-axisymmetric process loads. In fact, the analysis of a set of steels welds completed on an industrial inertia welder equipped with a monitoring system capable of extracting in-process key measurements, such as strain and runout, close to the weld interface showed significant non-axisymmetric loads and a non-negligible runout. These phenomena can have a significant impact on the repeatability and quality of welds, considering the strict geometrical tolerances on inertia welded components for aerospace applications. For this reason, a novel approach was developed to compute equivalent process loads from the measured strain data and it was possible to observe how large radial loads and moments are induced by the interaction of the workpieces when the system is analysed in non-idealised conditions. Then the loads obtained were applied to two models, a static and a dynamic representation of the inertia welder spindle, to analyse the system response and draw conclusions on the physical causes of the runout observed. It is finally important to note that the approach presented, even if developed specifically for IFW, is versatile enough to be applied to rotary friction welders of different configurations.

The outcomes of the study presented can be summarised as follows:

- The novel approach developed to calculate the equivalent loads generated by the interaction of the two workpieces during the welding achieved a good agreement with the experimental data, confirming its suitability as an inverse technique to calculate the actual process loads from auxiliary parameters easier to monitor during the welding (strain and runout). More specifically, the optimisation algorithm converged to solutions able to satisfy two objective functions: an FE representation of the monitoring system used to extract the experimental data, which ensured a load equivalency between the numerical solution and experiential data, and a static representation of the machine spindle, which compared the deflections induced by the equivalent process loads in a non-rotating rigid model of the spindle with the experimental data. The second objective function, required to avoid local minima in the solution, indicated how static effects could be sufficient to explain the runout observed in the machine spindle;
- The pressure distribution at the weld interface of the two workpieces calculated with the optimisation algorithm showed large variations, suggesting how the constant pressure distribution conventionally assumed could be not representative of the actual conditions during the welding but just a simplified assumption based on averaged conditions. This was particularly noticeable during the conditioning and burnoff phases, while it tended to flatten in the consolidation phase. The pressure variation can be connected to the imperfect contact of the workpieces during the conditioning phase and the unstable nature of the process in the burnoff phase and it could be particularly significant due to the risk of generating hot spots in the first phases of the welds at the localised pressure peaks;
- The equivalent process loads calculated from the pressure distribution at the weld interface showed how significant radial loads and bending moments should be expected when non-idealised contact conditions between the two workpieces are considered. In fact, along with the axial load and torque conventionally considered in IFW, radial loads and bending moments showing peaks up to 40% greater in magnitude than the experimental axial load and torque respectively were obtained;
- The non-axisymmetric interaction loads between the two workpieces combined with the flexibility of the spindle supports should be regarded as the major factor in the runout evolution during the weld. First a dynamic representation of the machine spindle was developed using 3D Timoshenko beam elements, Harris theory for the radial supports, the experimental data of angular speed and the equivalent process loads calculated with the optimisation algorithm. Then the results of this model were compared against the outcomes of the static model used in the optimisation and it was possible to conclude that no noticeable rotordynamic effects influenced the response of the system.

CRediT authorship contribution statement

Luca Raimondi: Methodology, Investigation, Formal analysis, Data curation, Visualization, Software, Writing - original draft. **Christopher J. Bennett:** Conceptualization, Methodology, Writing - review & editing, Supervision, Funding acquisition. **Andres**

(a)

(b)

(caption on next page)
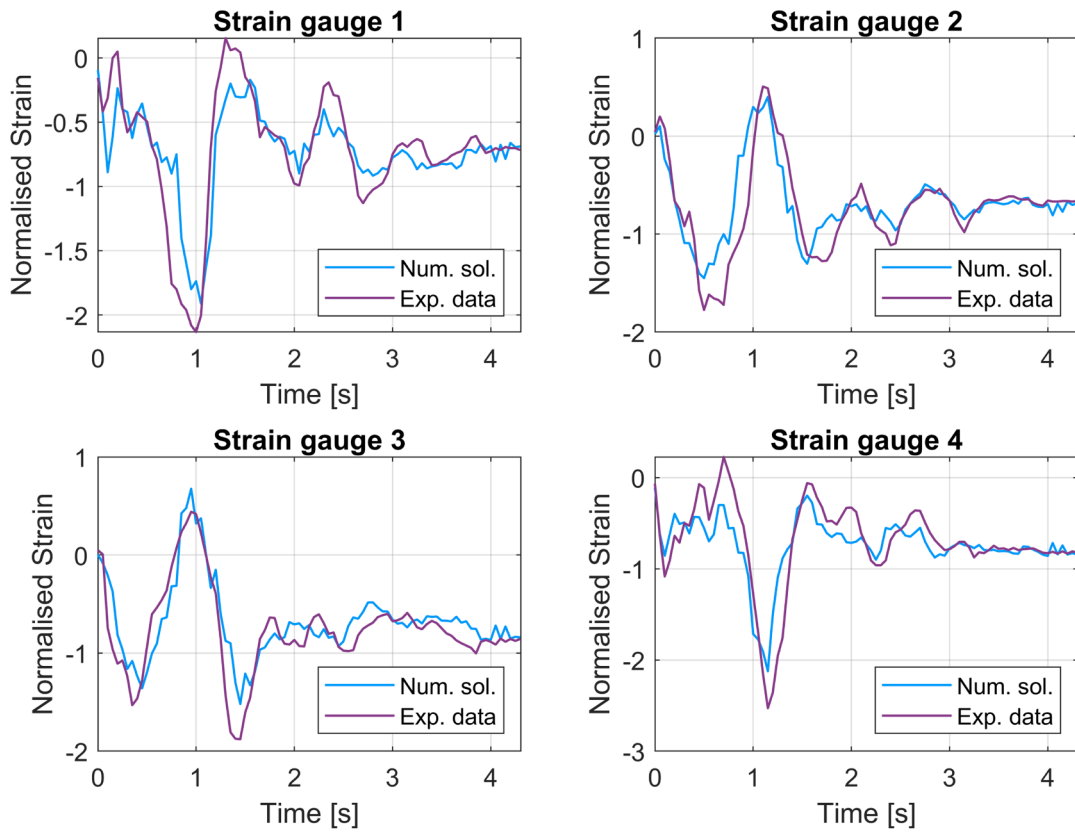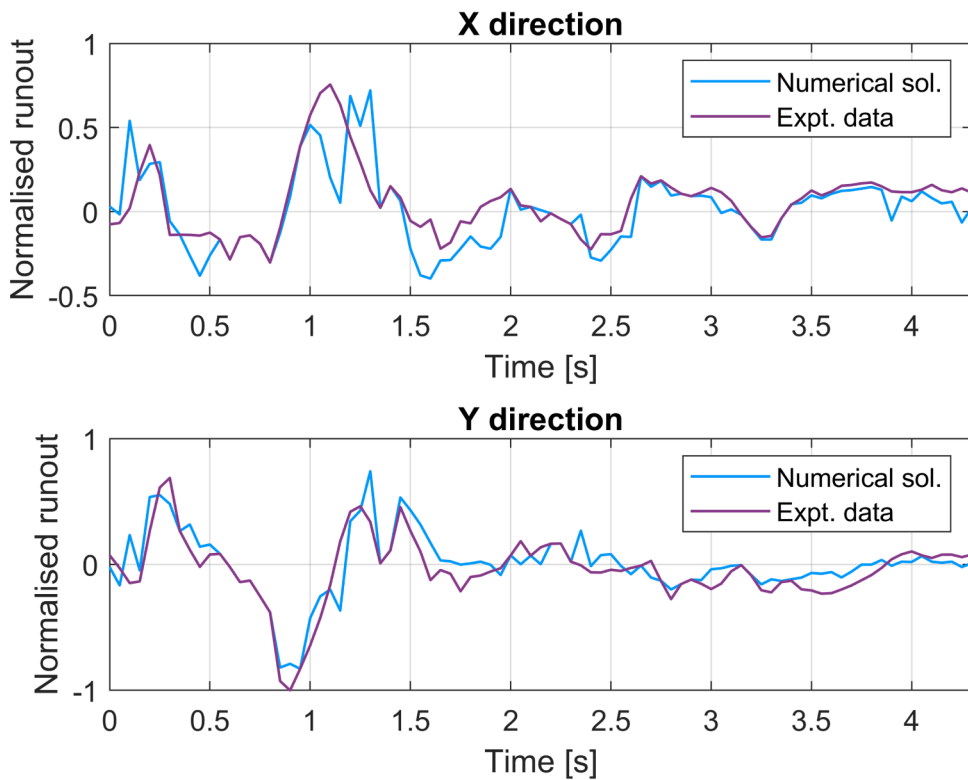
Fig. 13. Comparison between the experimental data and the numerical data computed with the optimisation: (a) Strain comparison at four locations 90° apart around the backup's neck; (b) Spindle runout comparison for the two orthogonal directions, X and Y.
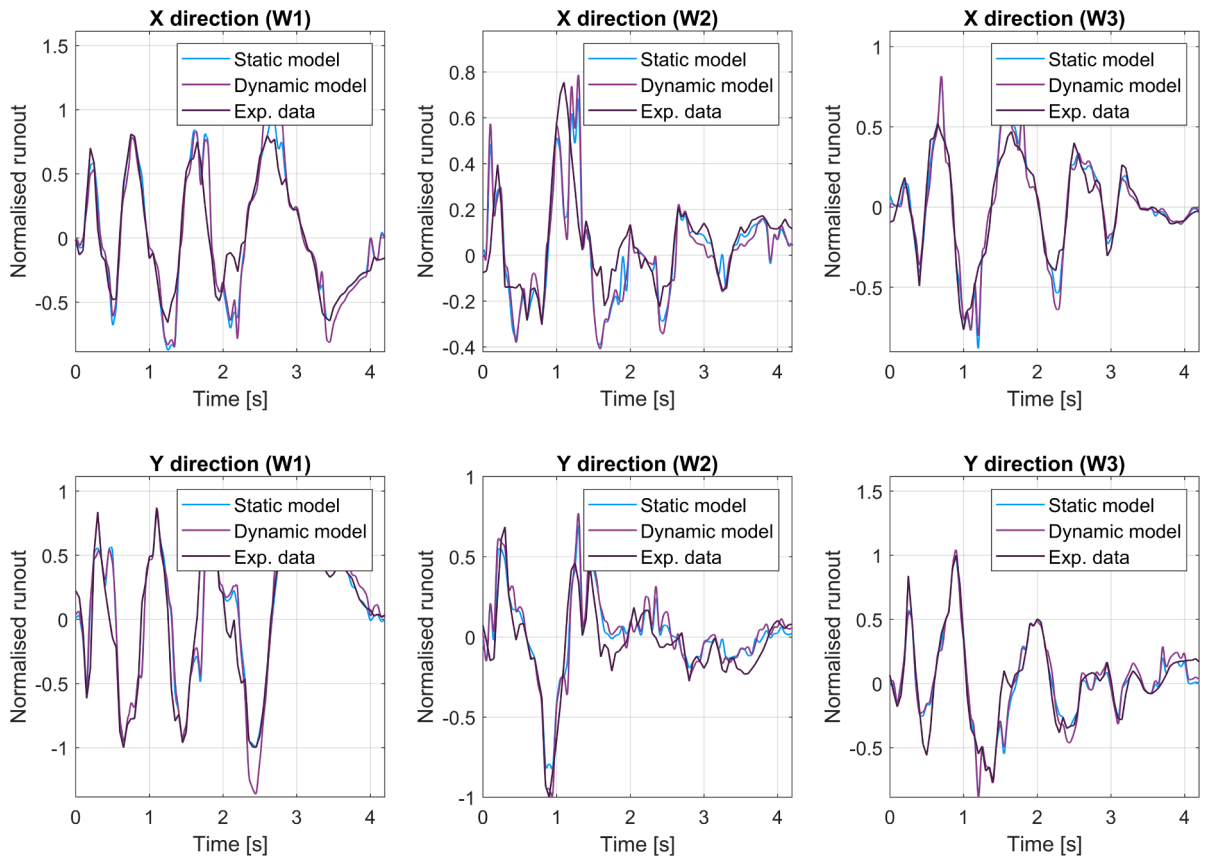
Fig. 14. Comparison of the radial runout obtained with the static and dynamic models and the experimental data for three welds (W1, W2, W3) completed with the same process parameters.
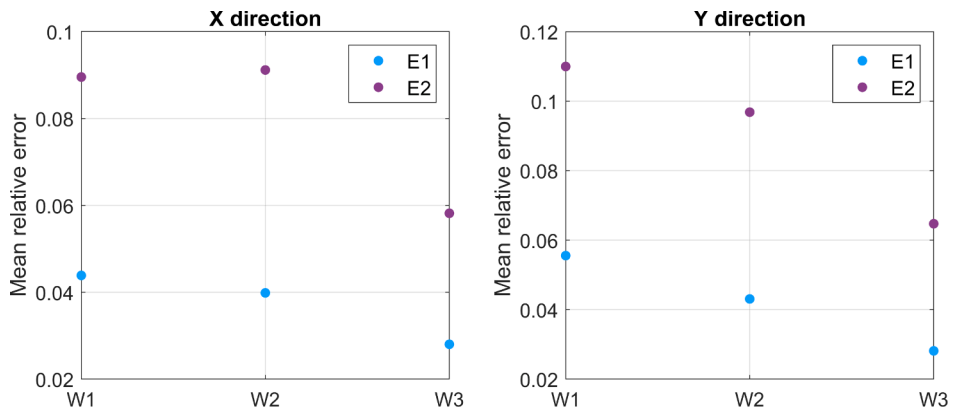
Fig. 15. Analysis of the mean relative error between static and dynamic model (E1) and between dynamic model and experimental data (E2) for the three welds analysed (W1, W2, W3).

Declaration of Competing Interest

The authors declare that they have no known competing financial interests or personal relationships that could have appeared to influence the work reported in this paper.

Acknowledgements

References

 [1] M. Attallah, M. Preuss, Inertia friction welding (IFW) for aerospace applications, in: Welding and Joining of Aerospace Materials, Woodhead Publishing, 2012, pp. 25–74.
 [2] O.N. Senkov, D.W. Mahaffey, D.J. Tung, W. Zhang, S.L. Semiatin, Efficiency of the inertia friction welding process and its dependence on process parameters, Metallurgical and Materials Transactions A 48 (2017) 3328–3342.
 [3] H. Cao, L. Niu, S. Xi, X. Chen, Mechanical model development of rolling bearing-rotor systems: A review, Mechanical Systems and Signal Processing 102 (2018) 37–58.
 [4] S. Xi, H. Cao, X. Chen, Dynamic modeling of spindle bearing system and vibration response investigation, Mechanical Systems and Signal Processing 114 (2019) 486–511.
 [5] Y. Ishida, T. Yamamoto, Linear and Nonlinear Rotordynamics: A Modern Treatment with Applications, 2nd ed., 2012.
 [6] A.D. Dimarogonas, S.A. Paipetis, T.G. Chondros, Analytical Methods in Rotor Dynamics, 2013.
 [7] T.A. Harris, M.N. Kotzalas, Rolling Bearing Analysis: Essential Concepts of Bearing Technology, 5th ed., CRC Press, 2006.
 [8] E. Abele, Y. Altintas, C. Brecher, Machine tool spindle units, CIRP Annals – Manufacturing Technology 59 (2010) 781–802.
 [9] T.Y. Chen, W.J. Wei, J.C. Tsai, Optimum design of headstocks of precision lathes, International Journal of Machine Tools and Manufacture 39 (1999) 1961–1977.
[10] Y. Cao, Y. Altintas, Modeling of spindle-bearing and machine tool systems for virtual simulation of milling operations, International Journal of Machine Tools and Manufacture 47 (2007) 1342–1350.
[11] Y. Altintas, Y. Cao, Virtual design and optimization of machine tool spindles, CIRP Annals 54 (2005) 379–382.
[12] H. Cao, T. Holkup, Y. Altintas, A comparative study on the dynamics of high speed spindles with respect to different preload mechanisms, International Journal of Advanced Manufacturing Technology 57 (2011) 871–883.
[13] Y. Ciou, C. Lee, Controllable preload spindle with a piezoelectric actuator for machine tools, International Journal of Machine Tools and Manufacture 139 (2019) 60–63.
[14] M. Namazi, Y. Altintas, T. Abe, N. Rajapakse, Modeling and identification of tool holder-spindle interface dynamics, International Journal of Machine Tools and Manufacture 47 (2007) 1333–1341.
[15] H. Cao, B. Li, Z. He, Chatter stability of milling with speed-varying dynamics of spindles, International Journal of Machine Tools and Manufacture 52 (2012) 50–58.
[16] M.R. Movahhedy, P. Mosaddegh, Prediction of chatter in high speed milling including gyroscopic effects, International Journal of Machine Tools and Manufacture 46 (2006) 996–1001.
[17] M. Postel, O. Özsahin, Y. Altintas, High speed tooltip frf predictions of arbitrary tool-holder combinations based on operational spindle identification, International Journal of Machine Tools and Manufacture 129 (2018) 48–60.
[18] X. Zhang, Q. Han, Z. Peng, F. Chu, A comprehensive dynamic model to investigate the stability problems of the rotor-bearing system due to multiple excitations, Mechanical Systems and Signal Processing 70–71 (2016) 1171–1192.
[19] H. Wang, Q. Han, D. Zhou, Nonlinear dynamic modeling of rotor system supported by angular contact ball bearings, Mechanical Systems and Signal Processing 85 (2017) 16–40.
[20] K. Xu, B. Wang, Z. Zhao, F. Zhao, X. Kong, B. Wen, The influence of rolling bearing parameters on the nonlinear dynamic response and cutting stability of high-speed spindle systems, Mechanical Systems and Signal Processing 136 (2020).
[21] D. Lachowicz, C. Bennett, D. Axinte, S. Lowth, A. Walpole, C. Hannon, On the influence of tooling behaviour over axial shortening mechanisms in linear friction welding of titanium alloys and modelling plasticisation effects, International Journal of Machine Tools and Manufacture 161 (2021), 103674.
[22] L. Raimondi, C.J. Bennett, D. Axinte, A. Gameros, P.A. Stevens, Development of a novel monitoring system for the in-process characterisation of the machine and tooling effects in Inertia Friction Welding, Mechanical Systems and Signal Processing 18 (2020).
[23] W. Li, A. Vairis, M. Preuss, T. Ma, Linear and rotary friction welding review, International Materials Reviews 61 (2016) 71–100.
[24] Y. Cao, Y. Altintas, A general method for the modeling of spindle-bearing systems, Journal of Mechanical Design, Transactions of the ASME 126 (2004) 1089–1104.
[25] W. Jacobs, R. Boonen, P. Sas, D. Moens, The influence of the lubricant film on the stiffness and damping characteristics of a deep groove ball bearing, Mechanical Systems and Signal Processing 42 (2014) 335–350.